

HERMES: A STATISTICAL MEASUREMENT OF THE REDSHIFT DISTRIBUTION OF HERSCHEL-SPIRE SOURCES USING THE CROSS-CORRELATION TECHNIQUE

K. MITCHELL-WYNNE¹, A. COORAY^{1,2}, Y. GONG¹, M. BÉTHERMIN³, J. BOCK^{2,4}, A. FRANCESCHINI⁵, J. GLENN^{6,7},
 M. GRIFFIN⁸, M. HALPERN¹⁶, S. J. OLIVER¹⁴, M. J. PAGE⁹, I. PÉREZ-FOURNON^{10,11}, M. ROWAN-ROBINSON¹², D. SCOTT¹⁶,
 J. SMIDT¹, M. VACCARI⁵, L. VIGROUX¹³, L. WANG¹⁴, J. L. WARDLOW¹, G. WRIGHT¹⁵, M. ZEMCOV^{2,4}

Draft version November 3, 2018

ABSTRACT

The wide-area imaging surveys with the *Herschel* Space Observatory at sub-mm wavelengths have now resulted in catalogs of order one hundred thousand dusty, star-burst galaxies. These galaxies capture an important phase of galaxy formation and evolution, and their properties provide important clues to the nature of dusty star-formation and the role of galaxy mergers in triggering such star-formation in distant galaxies. Unfortunately, the redshift distribution of these galaxies, $N(z)$, is still mostly uncertain due to limitations associated with counterpart identification at optical wavelengths and spectroscopy followup. We make a statistical estimate of $N(z)$ using a clustering analysis of sub-mm galaxies detected at each of 250, 350 and 500 μm from the Herschel Multi-tiered Extragalactic Survey (HerMES) centered on the Boötes field. We cross-correlate *Herschel* galaxies against galaxy samples at optical and near-IR wavelengths from the Sloan Digital Sky Survey (SDSS), the NOAO Deep Wide Field Survey (NDWFS) and the Spitzer Deep Wide Field Survey (SDWFS). We create optical and near-IR galaxy samples based on their photometric or spectroscopic redshift distributions and test the accuracy of those redshift distributions with similar galaxy samples defined with catalogs of the Cosmological Evolution Survey (COSMOS), as the COSMOS field has superior spectroscopy coverage. We model-fit the clustering auto and cross-correlations of *Herschel* and optical/IR galaxy samples to estimate $N(z)$ and clustering bias factors. The $S_{350} > 20$ mJy galaxies have a bias factor varying with redshift as $b(z) = 1.0^{+1.0}_{-0.5}(1+z)^{1.2^{+0.3}_{-0.7}}$. This bias and the redshift dependence is broadly in agreement with galaxies that occupy dark matter halos of mass in the range of 10^{12} to $10^{13} M_{\odot}$. We find that the redshift distribution peaks around $z \sim 0.5$ to 1 for galaxies selected at 250 μm with an average redshift of $\langle z \rangle = 1.8 \pm 0.2$. For 350 and 500 μm -selected SPIRE samples the peak shifts to higher redshift, but the average redshift remains the same with a value of 1.9 ± 0.2 . We compare our clustering-based $N(z)$ results to sub-mm galaxy model predictions in the literature, and with an estimate of $N(z)$ using a stacking analysis of COSMOS 24 μm detections, and find they are in broad agreement.

Subject headings: submillimeter: galaxies — Galaxies: evolution — Galaxies: high-redshift

¹ Dept. of Physics & Astronomy, University of California, Irvine, CA 92697

² California Institute of Technology, 1200 E. California Blvd., Pasadena, CA 91125

³ Institut d'Astrophysique Spatiale (IAS), bat121, F-91405 Orsay, France; Université Paris-Sud 11 and CNRS (UMR8617)

⁴ Jet Propulsion Laboratory, 4800 Oak Grove Drive, Pasadena, CA 91109

⁵ Dipartimento di Astronomia, Università di Padova, vicolo Osservatorio, 3, 35122 Padova, Italy

⁶ Dept. of Astrophysical and Planetary Sciences, CASA 389-UCB, University of Colorado, Boulder, CO 80309

⁷ Center for Astrophysics and Space Astronomy 389-UCB, University of Colorado, Boulder, CO 80309

⁸ School of Physics and Astronomy, Cardiff University, Queens Buildings, The Parade, Cardiff CF24 3AA, UK

⁹ Mullard Space Science Laboratory, University College London, Holmbury St. Mary, Dorking, Surrey RH5 6NT, UK

¹⁰ Instituto de Astrofísica de Canarias (IAC), E-38200 La Laguna, Tenerife, Spain

¹¹ Departamento de Astrofísica, Universidad de La Laguna (ULL), E-38205 La Laguna, Tenerife, Spain

¹² Astrophysics Group, Imperial College London, Blackett Laboratory, Prince Consort Road, London SW7 2AZ, UK

¹³ Institut d'Astrophysique de Paris, UMR 7095, CNRS, UPMC Univ. Paris 06, 98bis boulevard Arago, F-75014 Paris, France

¹⁴ Astronomy Centre, Dept. of Physics & Astronomy, University of Sussex, Brighton BN1 9QH, UK

¹⁵ UK Astronomy Technology Centre, Royal Observatory, Blackford Hill, Edinburgh EH9 3HJ, UK

¹⁶ Department of Physics & Astronomy, University of British Columbia, 6224 Agricultural Road, Vancouver, BC V6T 1Z1, Canada

1. INTRODUCTION

The redshift distribution of the dusty, star-forming galaxies detected by the Spectral and Photometric Imaging Receiver (SPIRE; Griffin et al. 2010) aboard the *Herschel Space Observatory*¹⁷ (Pilbratt et al. 2010) at sub-mm wavelengths has yet to be determined observationally. The low spatial resolution of *Herschel*-SPIRE observations complicate an easy identification of counterparts at optical and near-IR wavelengths. Moreover, the optical emission from these starbursting galaxies is highly extinguished and could potentially bias optical spectroscopy observations to low-redshift bright galaxies. Instead of optical or IR spectroscopy, mm and sub-mm wave spectroscopy can be pursued targeting fine-structure and molecular lines such as CO and CII. Such measurements, unfortunately, are currently limited to a handful of the brightest sources – mostly the rarely lensed sub-mm galaxies (e.g., Lupu et al. 2010; Scott et al. 2011; Riechers et al. 2011; Harris et al. 2012) as existing instrumental capabilities do not allow large CO or CII surveys of typical sub-mm galaxies.

A statistical approach based on the photometry alone, using SPIRE colors, was considered in Amblard et al. (2010; see also Lapi et al. 2011), but such techniques are subject to uncertainties on the assumed spectral energy distribution (SED) of the galaxies at sub-mm wavelengths. These generally involve isothermal SED models, where the redshift distribution is degenerate with the assumed dust temperature distribution. Here we pursue a second statistical approach to measure the SPIRE galaxy redshift distribution using the spatial clustering of the sub-mm population relative to clustering of galaxies with an a priori known redshift distribution (Schneider et al. 2006; Newman 2008; Zhang et al. 2010). The unknown sub-mm redshift distribution can be estimated via the strength of its cross-correlation relative to galaxy samples of known redshifts. Modeling also requires that the clustering bias factors of all galaxies be determined jointly through a combination of auto and cross-correlation functions. The key advantage of this technique is that it does not require cross-identification of SPIRE sources in optical and IR catalogs.

For this study we make use of the data from the *Herschel* Multi-tiered Extragalactic Survey (HerMES; Oliver et al. 2012) which imaged a large number of well-known fields with existing multi-wavelength ancillary data with SPIRE. To cross-correlate against SPIRE-selected galaxies, we make use of near-IR selected galaxy samples from *Spitzer* observations based on the 1.6 micron “bump”, which has long been established as a viable redshift indicator (Sawicki 2002; Simpson & Eisenhardt 1999; Wright & Fazio 1994). The bump results from the fact that the H^- absorption in stellar atmospheres is minimally opaque at 1.6 μm . This leads to a bump in the spectral energy distributions of cool stars at 1.6 μm (John 1988) that is nearly ubiquitous in galaxy spectra. For $z > 0$, the wavelength at which the bump in the SED peaks allows for a redshift determination based on the colors in IRAC channels between 3.6 and 8 μm and covering the redshift range of 1 to 2.5. We complement these

“bump” galaxy samples with a 24 μm and an r -band based sample of dust obscured galaxies, which has a redshift distribution that peaks around $z \sim 2.3$ (Dey et al. 2008). We also make use of optical-selected galaxy samples with SDSS spectroscopic and photometric redshifts out to about 0.7.

The paper is organized as follows: In Section 2 we describe source selection in SPIRE and galaxy sample selection with IRAC and MIPS bands complemented with optical data to remove outliers. In Section 3 we describe the redshift distribution of the galaxy samples used for the cross-correlation analysis, and in Section 4 we describe the cross-clustering measurements. Model fits are presented in Section 5. In Section 6 we present $N(z)$ and $b(z)$, and discuss our results. We assume a flat- Λ CDM cosmological model and fix cosmological parameters to the best-fit values of $\Omega_m = 0.27$, $\Omega_b = 0.046$, $\sigma_8 = 0.81$, $n_s = 0.96$ and $h = 0.71$ when doing MCMC model fits (Komatsu et al. 2011).

2. SPIRE SOURCE AND GALAXY SAMPLE SELECTION

2.1. *Herschel*-SPIRE sample

The HerMES SPIRE source catalogs used for this analysis comes from a combined analysis involving both a direct source extraction and an attempt to account for blending at 350 and 500 μm wavelengths given the positions of 250 μm detections (Wang et al. in prep). The method updates the source extraction pursued by HerMES at each of the three SPIRE bands independently that ignored issues associated with blending at longer wavelengths (Smith et al. 2011).

In order to maximize the overlap with multi-wavelength data, we concentrate our study on the Boötes field with HerMES SPIRE data covering 12.5 deg². The field has been imaged with *Spitzer* IRAC as part of the *Spitzer* Deep Wide Field Survey (SDWFS; Ashby et al. 2009) and from the ground with optical to near-IR observations as part of the NOAO Deep Wide Field Survey (NDWFS; Jannuzi and Dey 1999), with coverage also provided by the Sloan Digital Sky Survey (SDSS; Abazajian et al. 2009).

For this study we selected sources with a flux density greater than 20 mJy in the Boötes field. We find in excess of 22,000 sources in each band covering the entire 12.5 deg² of SPIRE observations, while 3775, 3243, 958 galaxies were used in the cross-correlation study in an area of 6.7 deg², where various ancillary data best overlap, at 250 μm , 350 μm and 500 μm , respectively.

2.2. IRAC Sample Selection and Star-Galaxy Separation

Using the SDWFS data combined with ground-based K-band data from NDWFS, we generated three different catalogs of 1.6 μm -bump sources based on the IRAC channel where the SED peaks. These three samples are as follows: bump-1 with a peak in the 3.6 μm channel ($0.5 \lesssim z \lesssim 1.5$), bump-2 peaking in the 4.5 μm channel ($0.8 \lesssim z \lesssim 2.2$), and bump-3 with a peak at 5.8 μm ($1.5 \lesssim z \lesssim 3.0$). Using the photometric redshifts computed via a template fitting method (Csabai et al. 2003) in the SDSS DR7 catalog, we also constructed two separate redshift distributions with $0 < z < 1$ peaks at $z \sim 0.3$ and 0.7.

¹⁷ *Herschel* is an ESA space observatory with science instruments provided by European-led Principal Investigator consortia and with important participation from NASA.

In order to establish catalogs of bump-1 to bump-3 galaxy populations we first had to remove stars and other contaminants from our optical and IR catalogs. This was done using a combination of infrared and optical data. We used the SDWFS four-epoch stacked catalog (Ashby et al. 2009) which contains all sources detected in the first channel of IRAC at or above 5σ . This catalog was matched with the NDWFS third data release catalog, and the SDSS catalog using a $2.5''$ matching radius. For sources with multiple matches ($<3\%$), magnitudes from the NDWFS catalog were then compared with the $3.6\mu\text{m}$ magnitude and entries with the most similar values were kept.

Stars and spurious sources were removed from the resulting merged catalog using various techniques. Vega magnitudes and $6''$ diameter aperture photometry are used throughout the star-galaxy separation unless otherwise noted. We employed a three stage process to remove stars from our catalog. An initial selection of sources with $[3.6] < 16$ were identified as stars. Using the combination of optical and IRAC photometry we further classify sources as stars that either satisfy $(B_w - I) > 2(I - [3.6]) - 1.65$, or $-1.65 > (B_w - I) - 2(I - [3.6]) > -3.35$ (Eisenhardt et al. 2004). The former criterion defines a sequence of *BIK* stars (Huang et al. 1997), and the latter a sequence of giant stars (Johnson 1966; Bessell & Brett 1988). Lastly, for IRAC sources without optical counterparts, we used a binning method that involved only the IRAC bands (Waddington et al. 2007). Three flux density bins were defined with the criteria $[3.6] \leq 19.5$, $19.5 < [4.5] \leq 20.0$ and $[4.5] \leq 23$, with color cuts $[3.6] - [4.5] < -0.35$, -0.30 and -0.25 respectively; all sources satisfying these criteria were assumed to be stars. The results of these extractions are shown in Fig. 1.

2.3. Bump, DOG and SDSS Selections

From our resulting merged and star-subtracted catalog, we invoked simple color constraints to classify three different classifications of bump sources and dust-obscured galaxies (DOGs; Dey et al. 2008), using $4''$ aperture diameter photometry. Bump-1, bump-2 and bump-3 sources each display excess emission in IRAC channels 1, 2 and 3, respectively. Bump-1 sources were selected using the criteria $K - [3.6] > 0.1$ and $[3.6] - [4.5] < 0$; bump-2 with $K - [3.6] > 0$, $[3.6] - [4.5] > 0$ and $[4.5] - [5.8] < 0$; bump-3 with $[3.6] - [4.5] > 0$, $[4.5] - [5.8] > 0$ and $[5.8] - [8] < 0$. The number of bump-1 sources in the SDWFS catalogs were found to be $\sim 1.3 \times 10^4$ at the 5σ detection limit of the 3.6 micron channel of the IRAC instrument. Bump-2 source identification yielded 6.5×10^3 galaxies, while the bump-3 catalog contains 4×10^3 galaxies.

We also make use of a sample of dust obscured galaxies (DOGs; Dey et al. 2008), selected with $24\mu\text{m}$ *Spitzer*-MIPS and optical R-band data to have extreme red colors from dust obstruction with $F_{24}/F_R > 1000$ (where F_{24} is the $24\mu\text{m}$ flux density), or equivalently $R - [24] \geq 14$ and $F_{24} \geq 0.3$ mJy ($\approx 6\sigma$; Dey et al. 2009). We found that a total of 2838 galaxies satisfied the selection criteria. Based on spectroscopic followup, they are now known to have a mean redshift around $z \sim 2.3$. We make use of the full, broad redshift distribution for this sample spanning the range of $0.5 < z < 3.5$ with a peak around $z \sim 2$

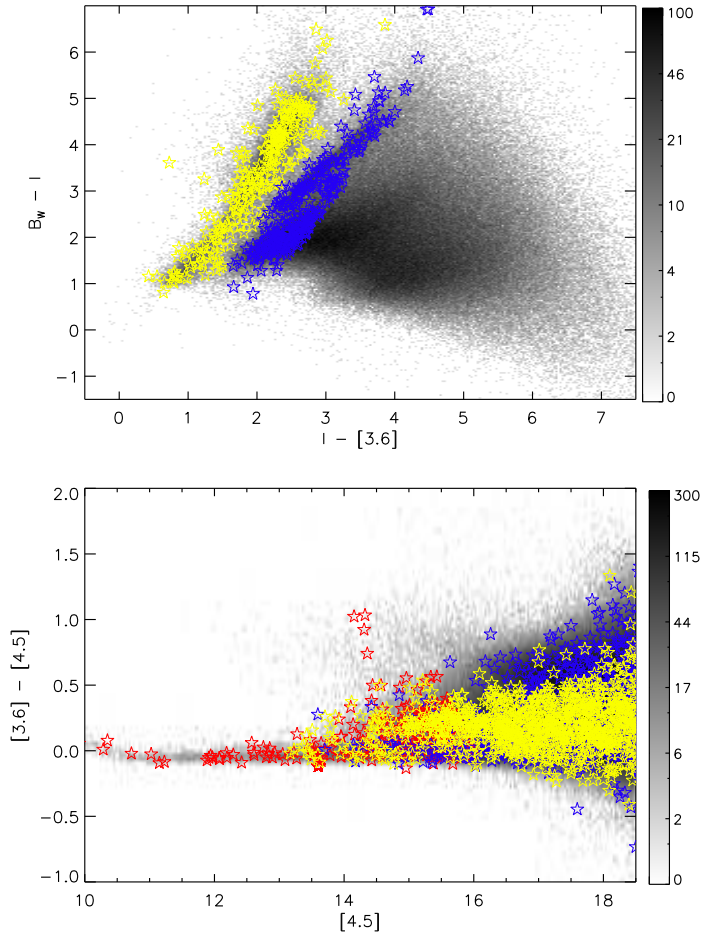


FIG. 1.— Color-color (top; $B_w - I$ vs. $I - [3.6]$) and color-magnitude (bottom; $[3.6] - [4.5]$ vs. $[4.5]$) density plots of sources (both stars and galaxies) in our Boötes field catalogs. Red stars indicate the $3.6\mu\text{m}$ magnitude selection for stars, while giant stars are depicted as yellow stars, and *BIK* sequence as blue stars (see Section 2.2 for details). Only a fraction of the sources identified as stars are plotted to avoid over-crowding in the plots. Black points are the resulting galaxies.

from a similar identification of DOGs in the COSMOS field (see Section 3 and Fig. 2) for the present analysis. These dust-obscured galaxies have been suggested to be an intermediary phase of the evolution of quasi-stellar objects from gas-rich mergers (Dey 2009). They have also been shown to be strongly clustered and are believed to be progenitors of massive ($3-6L_*$) galaxies at low redshift (Browdin et al. 2008).

Finally, to cover the redshift range of $0 < z < 0.7$ efficiently we also selected optical galaxies from SDSS with $B - I > 3$ and $I - R < -0.9$. They have photometric redshifts, individually determined with SED fits to SDSS photometry, in the above range. We make use of 8×10^3 SDSS galaxies and we consider two sub-samples peaking at $z \sim 0.2$ and 0.5 with roughly equal numbers. The six galaxy samples (3 bump catalogs, DOGs, and two SDSS samples) provide adequate redshift coverage over the range of $0 < z < 3$.

3. COSMOS PHOTO-Z AND SPEC-Z

While we are able to generate large samples of galaxies to cross-correlate against the SPIRE catalogs of the

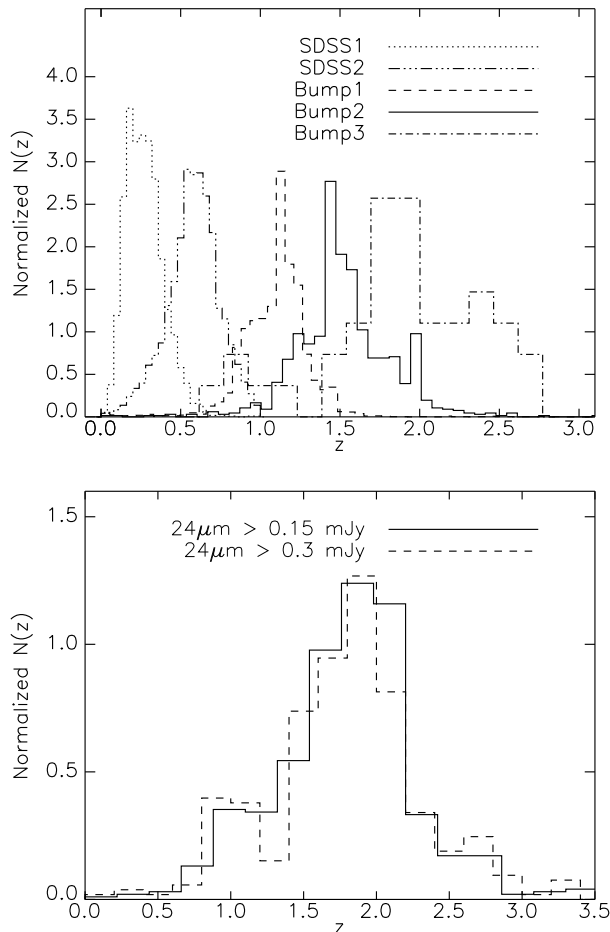


FIG. 2.— $N(z)$ distribution obtained from SDSS photometric redshifts in the Boötes field and bump-1 to -3 (top plot) and DOGs (bottom plot) redshift distributions from the COSMOS field. We assume the latter four redshift distributions measured directly in COSMOS are also applicable for galaxy samples under the same color selection criteria in the Boötes field.

Boötes field, the existing spectroscopic and photometric redshift information in the Boötes field is not adequate to establish the redshift distributions of the *Spitzer* galaxy samples. For that we turn to data in the Cosmological Evolution Survey (COSMOS; Scoville et al. 2006; Capak et al. 2007) where we can select similar galaxy samples as the Boötes field and using the same depth and color criteria. For those galaxies we are able to use either the existing spectroscopic or the photometric redshifts from the public COSMOS catalog (Ilbert et al. 2009). We assume that the redshift distributions for galaxy samples in COSMOS is same as those of Boötes when interpreting clustering measurements from the wider Boötes area that overlaps with SPIRE.

The COSMOS field has extensive photometric redshift measurements over 2 deg^2 using 30 broad, intermediate and narrowband filters from space-based telescopes (Hubble, Spitzer, GALEX, XMM, Chandra) and ground-based telescopes (Subaru, VLA, ESO-VLT, UKIRT, NOAO, CFHT, and others). We used a public COSMOS source catalog containing $\sim 10^4$ spectroscopic redshifts, and $\sim 3 \times 10^5$ photometric redshifts that were computed using a χ^2 galaxy template-fitting technique (Ilbert et al. 2009). In both the Boötes and COSMOS

fields, we imposed the same brightness thresholds in the selection bands: for IRAC channel 1 and K-band, we rejected sources that were detected below the 5σ limit, and for IRAC channels 2 to 4 we rejected sources dimmer than the 50% completeness limits in each band. This ensured that we were probing equal depths between the fields.

Using the same selection methods described above, we were able to obtain $N(z)$ measurements for each of our different source classifications from the COSMOS source catalog (see Fig. 2). All of the bump sources have well defined redshift distributions, and the DOG distribution agrees well with the literature (see Fig. 1 in Dey (2009)). We identified 384 sources as DOGs in COSMOS, with $F_{24} > 0.3 \mu\text{Jy}$, and 683 with $F_{24} > 0.15 \mu\text{Jy}$, a number density consistent with statistics of the DOG population in other fields (Browdin et al. 2008).

4. ANGULAR CROSS-CORRELATION AND COVARIANCE MATRIX

To obtain the redshift distributions of SPIRE sources, we first cross-correlate the SDSS-selected sample, bumps and DOGs from the Boötes field against sub-mm sources in each SPIRE band from arcminute to degree angular scales. We also measure the auto-correlation functions of the galaxy and SPIRE samples, as these are needed to model-fit the clustering strength and to extract the unknown redshift distribution.

Using a bootstrap method, we establish the covariance matrix for each of the cross or auto-correlation functions, as an accounting of the covariance is needed to properly model-fit the clustering measurements. The angular cross-correlation function is modeled analytically using the COSMOS redshift distribution of the bump-1, bump-2, bump-3 and DOGs, while for SDSS galaxy samples we make use of the public photometric redshifts from SDSS DR-7 for each of the galaxies to obtain the sample distribution.

For simplicity we bin the unknown SPIRE redshift distribution over the redshift interval of 0 to 4 in 5 bins in redshift. To extract the best-fit values and uncertainties in the redshift distribution bins and the other parameters in the analytical model, we make use of a likelihood model fitting technique based on the Markov Chain Monte Carlo (MCMC) method.

In this section, we first discuss the method of modeling the angular cross-correlation w_{cross} using the redshift distribution of galaxies and the linear matter power spectrum. Then we describe the measurement of the w_{cross} as well as the covariance matrix from the galaxy samples.

4.1. Modeling the angular cross-correlation

The angular cross-correlation function w_{cross} for two galaxy samples is defined by

$$w_{\text{cross}}(\theta) = \langle \delta n_1(\hat{\phi}) \delta n_2(\hat{\phi}') \rangle, \quad (1)$$

where $\delta n_i(\hat{\phi}) = (n_i(\hat{\phi}) - \bar{n}_i) / \bar{n}_i$, and $n_i(\hat{\phi})$ is the number density of galaxies observed in direction $\hat{\phi}$ in the sky ($\theta = \phi - \phi'$), and \bar{n}_i is the mean number density of the galaxy sample i . δn_i can be decomposed in terms of clustering of galaxies and we ignore the few percent correction to clustering resulting from the lensing of sub-mm galaxies here.

The galaxy clustering term is

$$w_{gg}(\theta) = b_1 b_2 \int_0^{\chi_H} d\chi N_1(\chi) N_2(\chi) \quad (2)$$

$$\times \int_0^\infty \frac{k}{2\pi} P(\chi, k) J_0[kr(\chi)\theta],$$

where b_1 and b_2 , $N_1(\chi)$ and $N_2(\chi)$ are the galaxy bias and the normalized radial distribution for the two galaxy samples, respectively. $P(\chi, k)$ is the power spectrum of the dark matter, $J_0(x) = \sin(x)/x$ is the zero-order Bessel function, and χ and $r(\chi)$ are the radial comoving distance and the comoving angular diameter distance respectively ($r(\chi) = \chi$ in flat space). χ_H denotes the radial distance to the horizon. Note that $w_{gg}(\theta)$ would be zero if the two galaxy samples do not overlap.

When modeling the measurements, we make use of the linear theory power spectrum to describe $P(\chi, k)$ and focus only on modeling the measurements over the angular scales of $6'$ and above where the clustering is in the linear regime (Cooray et al. 2000). At these large angular scales, the 1-halo term makes less than a 1% correction to the correlation function and can be safely ignored.

4.2. The measurement and the covariance matrix of the angular cross-correlation

In practice, the angular cross-correlation function $w_{\text{cross}}(\theta)$ is defined as the fractional excess of the probability relative to a random distribution (Peebles 1980), and can be measured by the *pair counts* method from galaxy samples. There are several kinds of estimators that are proposed to measure the cross-correlation (Blake et al. 2006), the estimator we adopt here is the modified Landy-Szalay estimator which is derived from the auto-correlation (Landy & Szalay 1993),

$$w_{\text{cross}}(\theta) = \frac{D_1 D_2 - D_1 R_2 - D_2 R_1 + R_1 R_2}{R_1 R_2}, \quad (3)$$

where $D_1 D_2(\theta)$, $D_1 R_2(\theta)$, $D_2 R_1(\theta)$ and $R_1 R_2(\theta)$ are the normalized pair counts for data (D_i) and random (R_i) catalogs with separation θ .

We generate random un-clustered catalogs with varying catalog sizes that contain 5 to 10 times more sources than the observed samples, with a larger number of sources than in data catalogs to avoid biases coming from Poisson fluctuations. The angular cross-correlation extracted from the observational data and the theoretical estimation using the best-fit value (see next section) of the SPIRE distribution in the Boötes field are shown in Fig. 3. The auto- and cross-correlation for 250 μm , 350 μm and 500 μm of the SPIRE surveys are also shown in Fig. 4.

As outlined in the previous Section, to avoid biases coming from non-linear clustering, we only use $w(\theta)$ data from 0.1 to 1 degree to fit the model, since adding the 1-halo term with three or four extra parameters for the halo occupation number will result in extra degeneracies degrading the $N(z)$ estimates, consistent with theoretical suggestions in the literature (e.g., Neyrinck et al. 2006). Also keeping to scales larger than 0.1 degrees, we avoid the need to introduce a transfer function for $w(\theta)$ of SPIRE sources and their cross-correlations since at smallest scales close to the SPIRE point response

function, clustering is expected to be affected by source blending and issues related to map making. As studied in Cooray et al. (2010), at $\theta > 0.05$ degrees, there are no corrections to the measured $w(\theta)$.

To evaluate the covariance matrix of the angular correlation $w(\theta)$, we use a bootstrap method to generate 200 realizations for the galaxy samples. Then the covariance matrix of w_{cross} is

$$C_{ij} = \frac{1}{N-1} \sum_k^N [w_k(\theta_i) - \bar{w}(\theta_i)][w_k(\theta_j) - \bar{w}(\theta_j)], \quad (4)$$

where $N = 200$ is the number of the bootstrap realization, and $\bar{w}(\theta)$ is the average angular correlation for all bootstrap realizations at θ . The error of the angular correlation thus takes the form as $\sigma_w(\theta_i) = \sqrt{C_{ii}}$.

We use 9 logarithmic bins from 0.01 to 1 degree to calculate the angular auto and cross correlation and their covariance matrix. The model correlation and cross-correlation functions, w^{th} , are calculated for a given $N(z)$ and clustering bias factors (described in the next Section) and compared with measurements, w^{data} , using the covariance matrix from the data. In calculating w^{th} , we make use of the measured $N(z)$ of the SDSS, bumps and DOGs derived in the last section.

5. ESTIMATING THE SPIRE GALAXY REDSHIFT DISTRIBUTION

We employ a Markov Chain Monte Carlo (MCMC) technique to model-fit the SPIRE redshift distribution $N(z)$ of sources with flux densities greater than 20 mJy at each of the three wavelengths. Instead of parameterizing the unknown redshift distribution to a specific form, we pursue a model-independent approach by describing $N(z)$ with 5 values at 5 ‘‘pivot’’ redshifts $z_p = 0.1, 0.5, 1, 2$ and 3 , and set $N(z_p = 0) = 0$ and $N(z_p = 4) = 0$ to describe the two end points of the redshift distribution. The assumption that $N(z > 4) = 0$ does not bias our results since we only expect at most a few percent of the sub-mm galaxies to be located at $z > 4$. Furthermore, we do not have sensitivity to such high redshifts given the optical and near-IR galaxy samples we have used for the cross-correlation study are restricted to $z < 4$. To describe $N(z)$ when $0 < z < 4$, we linearly interpolate the fitted $N(z)$ distribution at each of the pivot redshifts z_p and use those linearly interpolated values between two pivots in our model fitting algorithm.

Before deciding on this description, we also considered a description of $N(z)$ that involved five bins in redshift with $N(z)$ taking the same value in each of the bins. We failed to obtain model-fits to the binned case since in the first bin $0 < z < z_1$, $N(z)$ prefers a value that is non-zero at z_1 , but zero at $z = 0$. The use of pivot redshifts and linear interpolation between pivots avoid the discontinuities that were present with the binned case leading to issues with the numerical integrations of the clustering in equation 2.

As discussed earlier related to equation 2, we also need to account for the clustering bias factor of galaxies and SPIRE sources relative to the linear matter power spectrum. Instead of keeping the bias in each of the bins as a free parameter, which leads to a large number of model parameters to be determined from the data, we assume a model for the galaxy bias as a function of redshift to

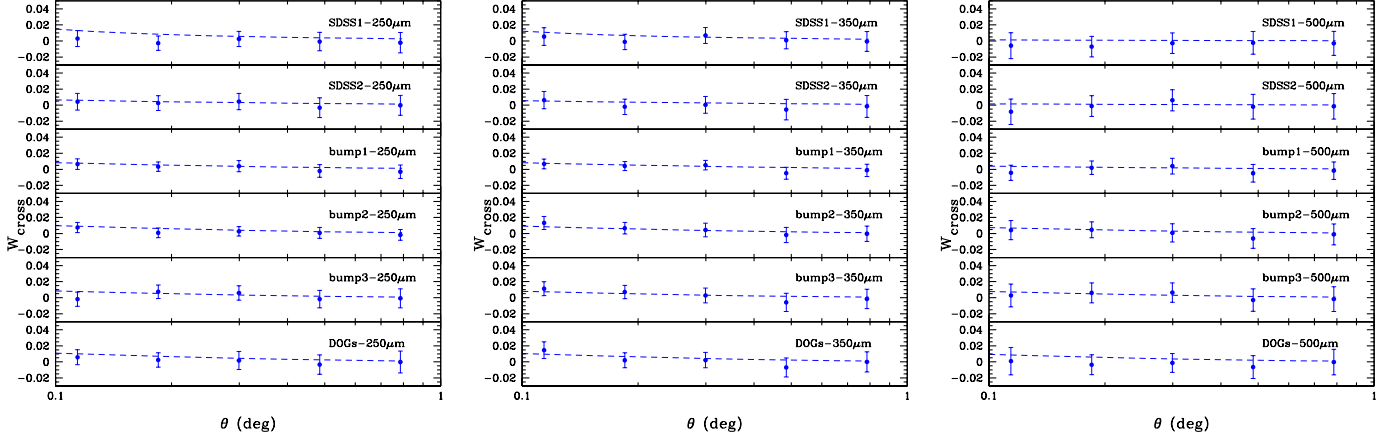


FIG. 3.— The angular cross-correlation between the 250, 350, and 500 μm of the SPIRE surveys and the SDSS1, SDSS2, bump1, bump2, bump3 and DOGs in the Boötes field. The 1σ error bars are derived from 200 bootstrap realizations. The blue dashed lines are the theoretical estimation of the angular cross-correlation using the best-fit value of the SPIRE redshift distribution.

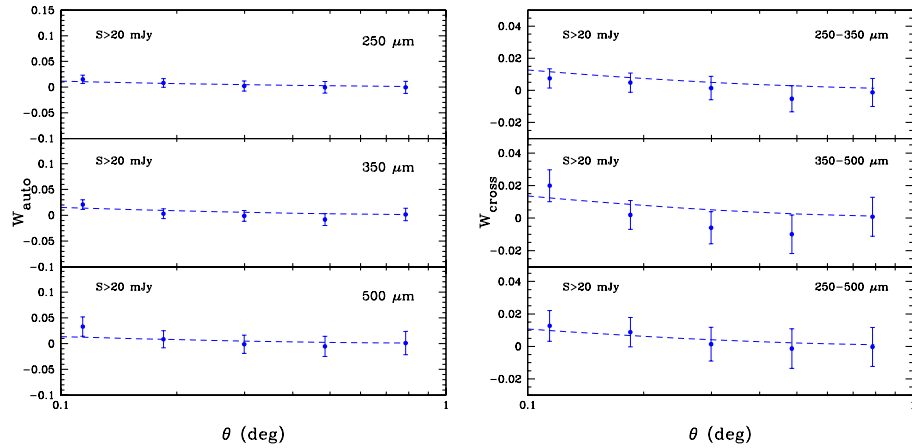


FIG. 4.— The angular auto- and cross-correlation for the 250, 350, and 500 μm SPIRE sources in the Boötes field. The 1σ error bars are derived from 200 bootstrap realizations. The blue dashed lines are the theoretical estimation using the best-fit value of the SPIRE redshift distribution.

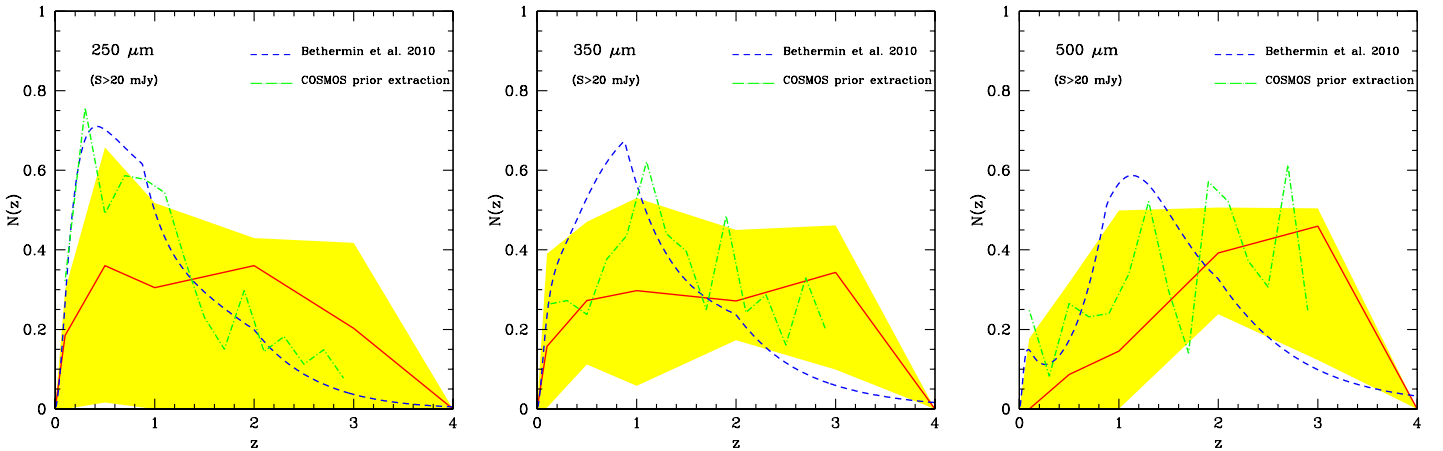


FIG. 5.— The best-fit normalized redshift distributions (red solid line) and 1σ error (yellow region) for sources with flux densities greater than 20 mJy for 250, 350 and 500 μm SPIRE bands using SDSS, bump-1 to bump-3, and DOGs catalogs in the Boötes field. The analytical model predictions on $N(z)$ from the literature (blue dashed line; Béthermine et al. 2010) for galaxies in the three SPIRE bands are also shown for comparison. The green line is a direct estimate of $N(z)$ using the combination of a stacking and a cross-identification analysis involving 24 μm MIPS and SPIRE sources from Béthermin et al. (2012).

be of the form

$$b(z) = b_0(1+z)^c, \quad (5)$$

where b_0 and c are free parameters to be determined from

data using the MCMC analysis. In addition to this model we also consider two other approaches with (i) $b(z) = b_0 + b_1 z$, a simple linear interpolation with redshift, and (ii) $b(z) = b_0$ when $z < 2$ and $b(z) = b_1$ when $z > 2$. We found results consistent within 1σ uncertainties of both $N(z)$ and $b(z)$ with the power-law form when using the linear relation, while in the binned case we found issues related to the discontinuity of the bias factor.

For optical and IR galaxy samples we assume each has an average bias factor and we do not account for the redshift evolution of the bias factor in each of the galaxy samples. This is a fair assumption since each of the samples has a redshift distribution that peaks at a given redshift and the broad distributions such as SDSS is sub-divided to two subsamples.

Altogether we have 13 free parameters in our MCMC fitting, which contains five parameters for the SPIRE redshift distribution and six bias parameters for SDSS-1, SDSS-2, bump-1, bump-2, bump-3, and DOGs and two parameters to describe the SPIRE galaxy bias and its evolution with redshift. While the redshift distribution and bias factor and evolution for SPIRE sources are different at each of the three SPIRE wavelengths, the bias factors for optical and IR-selected galaxies remain the same. Thus, the six bias parameters for the galaxy samples with assumed or known redshifts can be determined jointly from cross-correlation data at all three SPIRE wavelengths and their auto-correlation functions. We fix all the other cosmological parameters and assume the flat Λ CDM model as mentioned in Section 1.

We model-fit data following the χ^2 distribution estimated as

$$\chi^2 = \sum_{\text{datasets}} \Delta^T \mathbf{C}^{-1} \Delta, \quad (6)$$

where $\Delta = [w^{\text{data}}(\theta_1) - w^{\text{th}}(\theta_1), \dots, w^{\text{data}}(\theta_9) - w^{\text{th}}(\theta_9)]$, \mathbf{C} is the covariance matrix of $w(\theta)$, and “data” are the full angular cross-correlations for the SPIRE, SDSS-1, SDSS-2, bump-1, bump-2, bump-3 and DOGs (21 cross-correlations for each SPIRE band), and their auto-correlations in the Boötes field. The angular auto-correlation and the cross-correlation between the SPIRE and the SDSS1, SDSS2, bump1, bump2, bump3 and DOGs extracted from the observational data in the Boötes field are shown in Fig. 3 and Fig. 4 as examples.

The Metropolis-Hastings algorithm is applied in our MCMC fitting process, and we adopt an adaptive step-size Gaussian sampler given by Doran & Mueller (2004). The convergence criterion we take is discussed in Gelman & Rubin (1992). We generate 6 chains with about 10^5 points after the convergence process. At the end we resample the chains to get about 10000 points to illustrate the probability distribution of the parameters.

6. RESULTS AND DISCUSSION

In Fig. 5 we show the best-fit results and the 1σ errors of the redshift distribution $N(z)$ for the three SPIRE bands (see also Table 1 for the values). The redshift distributions are normalized such that $\int dz N(z) = 1$. The error bars are derived from the Markov chains, which are statistically estimated by the values of $N(z)$ calculated using each chain point at different redshifts. As shown by the errors of $N(z)$ at high redshift ($z > 3$), the galaxy

TABLE 1
THE BEST-FIT SPIRE REDSHIFT DISTRIBUTION AND BIAS PARAMETERS

$N(z)$	z-pivot	250 μm	350 μm	500 μm
N_1	0.1	$0.19^{+0.11}_{-0.19}$	$0.16^{+0.23}_{-0.15}$	$0.00^{+0.18}_{-0.00}$
N_2	0.5	$0.36^{+0.30}_{-0.34}$	$0.27^{+0.20}_{-0.16}$	$0.09^{+0.23}_{-0.09}$
N_3	1.0	$0.31^{+0.21}_{-0.31}$	$0.30^{+0.23}_{-0.24}$	$0.15^{+0.35}_{-0.15}$
N_4	2.0	$0.36^{+0.07}_{-0.36}$	$0.27^{+0.18}_{-0.10}$	$0.39^{+0.11}_{-0.15}$
N_5	3.0	$0.20^{+0.22}_{-0.20}$	$0.34^{+0.12}_{-0.24}$	$0.46^{+0.04}_{-0.34}$
Average Redshift $\langle z \rangle$		1.8 ± 0.2	1.9 ± 0.2	1.9 ± 0.2
Sub-mm Bias				
b_0		$1.0^{+0.8}_{-0.5}$	$1.0^{+1.0}_{-0.5}$	$0.9^{+0.6}_{-0.5}$
c		$1.1^{+0.4}_{-0.6}$	$1.2^{+0.3}_{-0.7}$	$1.1^{+0.5}_{-0.8}$

distribution can be larger from 250 μm to 500 μm bands, which implies there may be more high-redshift galaxies for the 500 μm band than the 250 μm and 350 μm bands. In Table 1 we also tabulate the average redshift of the SPIRE sources by calculating $\int dz z N(z)$ and these values range from 1.8 ± 0.2 at 250 μm to 1.9 ± 0.2 for 500 μm .

Two additional $N(z)$ predictions from the literature are also shown in the plot for comparison. The dashed line is a direct estimate of $N(z)$ from PSF-fitted extraction using 24 μm positions as a prior (B  thermin et al. 2012) and the green curve is a model prediction for the SPIRE redshift distribution (B  thermin et al. 2010). Our estimation for $N(z)$ at 250 μm band agree well with both the direct extraction based on 24 μm identifications and a model prediction, while we find some differences at 350 and 500 μm . However, given the large uncertainties in our binned $N(z)$ estimate these differences are statistically insignificant. We do find evidence that the 250 μm redshift distribution peaks at $z \sim 1$ while the peak is shifting to higher redshifts at 350 and 500 μm . We also find an excess of sources in the highest redshift bin when compared to the model prediction from B  thermin et al. (2010).

TABLE 2
BIAS FACTORS OF OPTICAL AND IR-SELECTED GALAXY SAMPLES

Sample	z-Range	bias
SDSS-1	$\approx 0-0.4$	$1.6^{+0.2}_{-0.2}$
SDSS-2	$\approx 0.3-0.7$	$1.1^{+0.2}_{-0.3}$
Bump-1	$\approx 0.8-1.5$	$2.0^{+0.3}_{-0.3}$
Bump-2	$\approx 1.2-2.0$	$2.3^{+0.4}_{-0.5}$
Bump-3	$\approx 1.6-2.5$	$2.0^{+0.8}_{-1.1}$
DOGs	$\approx 0.7-3.0$	$2.6^{+1.1}_{-1.9}$

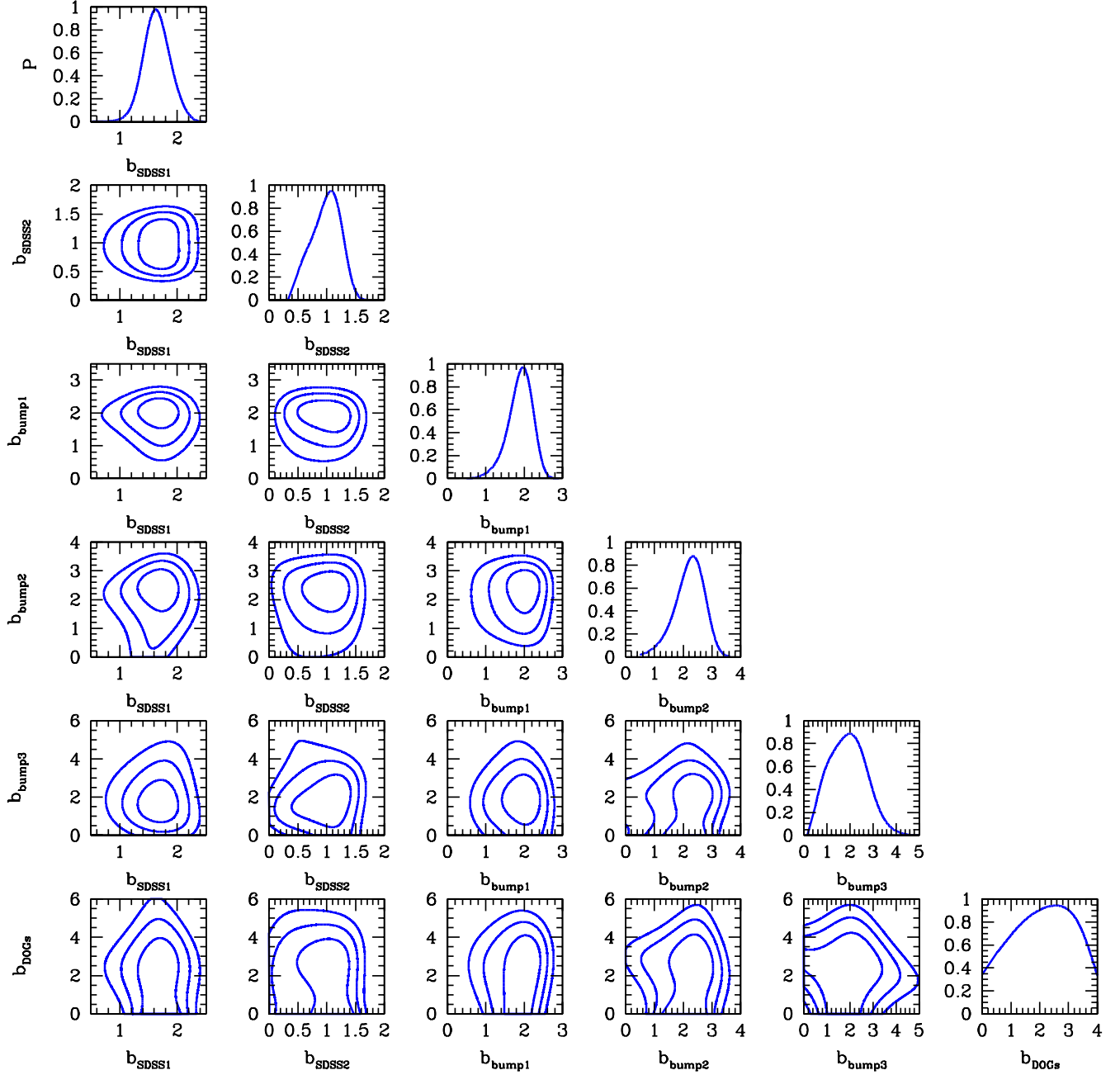


FIG. 6.— The one and two-dimensional probability distribution functions for bias parameters for all of the Boötes samples used throughout this paper. These bias parameters are estimated by combining the likelihoods from the MCMC chains of all three SPIRE bands. The 1 σ (68.3%), 2 σ (95.5%) and 3 σ (99.7%) uncertainties from the model-fits are shown in the two-dimensional error plots.

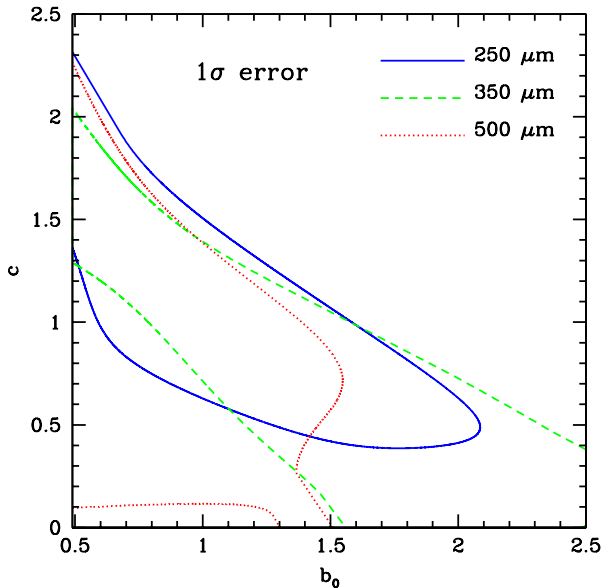


FIG. 7.— The 1σ contour maps of the bias parameters b_0 and c at 250, 350 and 500 μm with $S > 20\text{mJy}$ in the Boötes field.

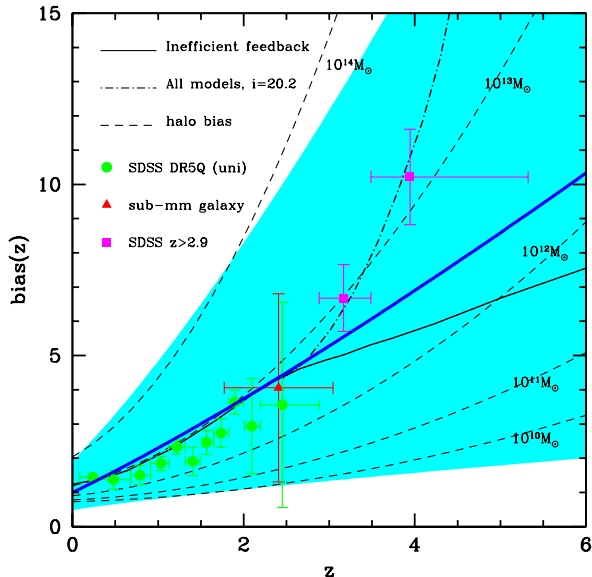


FIG. 8.— Clustering bias of $S_{350} > 20\text{ mJy}$ SPIRE sources as a function of redshift. The shaded region shows the 68% confidence level region allowed with blue solid line showing the best-fit $b(z)$ relation. For reference we plot the bias factor of dark matter halos as a function of the halo mass. The range allowed by the data over the range if $0 < z < 4$ is occupied by halos with mass $10 < \log M/M_\odot < 14$. We also show samples of merging galaxies and quasars from the literature (Hopkins et al. 2007; Ross et al. 2009), and two models for the evolution of the bias factor of merging galaxies (black solid and dash-dotted lines) from Hopkins et al. (2007) involving efficient (thick solid) and inefficient (thin solid) feedback.

In addition to $N(z)$ and bias factors of SPIRE-selected galaxies, we also measure the bias factors of optical and IR-selected galaxy samples that we have used for cross-correlations. In Fig. 6 we show the two-dimensional error plots while in Table 2 we list the best-fit bias values and their uncertainties. These results are obtained by combining the likelihoods from the MCMC chains of

all three SPIRE bands. These values are consistent with values quoted in the literature for the bias of these samples. For example, the dust-obscured galaxies have an estimated bias factor of 3.1 ± 0.5 (Brodwin et al. 2008), which can be compared to our estimate of $2.6^{+1.1}_{-1.9}$. While fully consistent with Brodwin et al. (2008) estimate our central value is lower than their value as we account for the full redshift distribution of these galaxies while their analysis assumed a redshift of 2 for the whole DOG sample in the Boötes field.

In Fig. 7 we show the 1σ contour maps of the bias factors of SPIRE sources at the three wavelengths (the values and uncertainties are listed in Table 1). We generally find that the SPIRE galaxy bias factors are consistent with $b(z) \sim 1 + z$. To understand further the evolution of the sub-mm galaxy bias factor, we plot the redshift dependence in Fig. 8, where we also plot the bias factor of dark matter halos at several halo masses from dwarf galaxy mass to galaxy cluster scales. The bias factors we find at all three wavelengths indicate a halo mass in the range of few times 10^{10} to few times $10^{13} M_\odot$. The SPIRE clustering analysis in Cooray et al. (2010) found a halo mass for sub-mm galaxies that is about $3 \times 10^{12} M_\odot$, under the assumption of a redshift distribution for the sub-mm galaxy population with a peak at $z \sim 2.3$, similar to the DOG redshift distribution in Figure 2. We now find a slightly lower bias factor and this is primarily due to the fact that the underlying redshift distribution of the SPIRE galaxies, especially at 250 μm , is peaking towards lower redshifts ($z \lesssim 1$). While the result here is for bright sub-mm sources that are individually detected, the model interpretation of the SPIRE anisotropy power spectrum by Amblard et al. (2011) found a minimum halo mass of $3 \times 10^{11} M_\odot$.

In Fig. 8 we also compare the SPIRE sub-mm galaxy bias factors to samples of merging galaxies and quasars from the literature (Ross et al. 2009). Our results are generally consistent with the possibility that SMGs and quasars trace similar evolutionary paths and the host halos correspond to dark matter halos that host \sim few L_\star ellipticals at $z \sim 0$. The exact mechanism on how the starburst galaxies seen in SPIRE feed the blackholes that result in the quasars and the subsequent feedback that suppresses star-formation remains uncertain.

In Fig. 8 we also plot two models for the evolution of the bias factor of merging galaxies from Hopkins et al. (2007). While these models have similar behavior at $z < 3$, differences exist at higher redshift. A clustering study of SPIRE-selected sub-mm galaxies at $z > 4$ on its own or as a cross-correlation with high-redshift quasars could potentially be used to understand the intricate role of starbursts and quasars and to separate the subsequent feedback processes.

7. SUMMARY

The wide-area sub-mm surveys with the SPIRE instrument aboard the *Herschel* Space Observatory have now led to catalogs of a few tens of thousand dusty, star-forming galaxies at 250, 350, and 500 μm . While some properties of this sub-mm source population are now understood, the redshift distribution of these galaxies $N(z)$ is not yet known observationally. We make a statistical estimate of $N(z)$ using a clustering analysis involving

the cross-correlation of sub-mm galaxies detected at each of 250, 350 and 500 μm from the Herschel Multi-tiered Extragalactic Survey (HerMES) centered on the Boötes field against samples of galaxies detected at optical and near-IR wavelengths from the Sloan Digital Sky Survey (SDSS), the NOAO Deep Wide Field Survey (NDWFS), and the Spitzer Deep Wide Field Survey (SDWFS).

We create optical and near-IR galaxy samples based on their photometric or spectroscopic redshift distributions and test the accuracy of those redshift distributions with similar galaxy samples defined with catalogs of the Cosmological Evolution Survey (COSMOS) as the COSMOS field has more spectroscopy coverage as well as a more accurate photometric redshift catalog. We model fit the clustering auto and cross-correlations of SPIRE and optical/IR galaxy samples at angular scales of 0.1 to 1 degrees, where clustering of each of the galaxy samples is expected to be linear with the amplitude determined by a bias factor and the redshift distribution of the sources. We make use of Markov Chain Monte Carlo (MCMC) method to sample $N(z)$ in 5 bins between $0 < z < 4$ as well as the bias factors. We find clear evidence of evolving redshift distributions as the wavelength increases from 250 μm to 500 μm . We also compare the measured redshift distribution to model predictions in the literature

and found general agreement. The SPIRE-selected sub-mm galaxy bias factor was found to scale with redshift as $b(z) \sim (1+z)^{[1.1-1.2] \pm 0.5}$ with values at $z \sim 2$ that are consistent with merging galaxies and quasars.

KMW, YG, AC and JLW are supported by NASA funds for US participants in Herschel through an award from JPL. SPIRE has been developed by a consortium of institutes led by Cardiff University (UK) and including Univ. Lethbridge (Canada); NAOC (China); CEA, LAM (France); IFSI, Univ. Padua (Italy); IAC (Spain); Stockholm Observatory (Sweden); Imperial College London, RAL, UCL-MSSL, UKATC, Univ. Sussex (UK); and Caltech/JPL, IPAC, Univ. Colorado (USA). This development has been supported by national funding agencies: CSA (Canada); NAOC (China); CEA, CNES, CNRS (France); ASI (Italy); MCINN (Spain); SNSB (Sweden); STFC (UK); and NASA (USA). The data presented in this paper will be released through the HeDaM Database in Marseille. This work made use of images and/or data products provided by the NOAO Deep Wide-Field Survey (Jannuzi and Dey 1999), which is supported by the National Optical Astronomy Observatory (NOAO). NOAO is operated by AURA, Inc., under a cooperative agreement with the National Science Foundation.

REFERENCES

- Ashby, M.L.N., et al. 2009, *ApJ*, 701, 428
 Amblard, A., et al. 2010, *A&A* 518, 9L
 Abazajian, et al. 2009, *ApJ Supplement Series*, 182, 543
 Bartelmann, M. & Schneider, P. 2001, *Physics Reports*, 340, 291
 Bessell, M.S., & Brett, J.M. 1988, *PASP*, 100, 1134
 Béthermin, M., Dole, H., Lagache, G., Le Borgne, D. & Penin, A. 2010, *A&A*, 529, A4
 Béthermin, et al. 2012, *A&A* in press.
 Blake, C., Pope, A., Scott, D. & Mobasher, B. 2006, *MNRAS*, 368, 732
 Browdin, M., et al. 2008, *ApJ*, 687, L65
 Capak, P.m et al. 2007, *ApJS*, 172, 99
 Csabai, I., et al. 2003, *AJ*, 125, 580
 Cooray, A. & Sheth, R. 2002, *Physics Report*, 372, 1
 Dey, A. 2009, *ASPC*, 408, 411
 Dey, A., et al. 2008, *ApJ*, 677, 943
 Dpran, M. & Mueller, C. M. 2004, *JCAP*, 0409, 003
 Eisenhardt, P.R., et al. 2004, *ApJ*, 154, 48
 Gong, Y. & Chen, X. 2007, *Phys. Rev. D*, 76, 123007
 Gelman, A. & Rubin, D. 1992, *Stat. Sci.*, 7, 457
 Harris, A. et al. 2012, *ApJ* submitted.
 Hopkins, P. F., Hernquist, L., Cox, T. & Keres, D. 2008, *ApJS*, 175, 356
 Huang, J., Cowie, L.L., Gardner, J.P., Hu, E.M., Songaila, A., & Wainscoat, R.J. 1997, *ApJ*, 476, 12
 Ilbert, O., et al. 2009, *ApJ*, 690, 1236
 Jannuzi, B. T. & Dey, A. 1999, *ASP Conference Series*, Vol. 191, p. 111
 John T.L. 1988, *A&A*, 193, 189
 Johnson, H.L. 1966, *ARA&A*, 4, 193
 Komatsu, E., et al. 2011, *ApJS*, 192, 18
 Landy, S. D. & Szalay, A. S. 1993, *ApJ*, 412, 64
 Lupu, R. E. et al. 2010, *arXiv.org:1009.5983*
 Moessner, R. & Jain, B. 1998, *MNRAS*, 294, L18
 Neyrinck, M. C., Szapudi, I. & Rimes, C. D. 2006, *MNRAS*, 370, L66
 Oliver, S. J. et al. 2012, *MNRAS* submitted.
 Peebles, P. J. E. 1980, *The Large-Scale Structure of the Universe*. Princeton Univ. Press, Princeton, NJ
 Pilbratt, G., et al. 2010, *A&A*, 518, L1
 Riechers, D. et al. 2011, *ApJ*, 733, L12
 Ross, N. P. et al. 2009, *ApJ*, 697, 1634
 Savage, R. S., & Oliver, S. 2007, *ApJ*, 661, 1339
 Sawicki, M. 2002, *AJ*, 124, 3050
 Schneider, M., Knox, L., Zhan, H., Connolly, A. 2006, *ApJ*, 651, 14
 Scoville, N. et al. *arXiv.org:astro-ph/0612305*
 Scott, K. S. et al. 2011, *ApJ*, 733, 29
 Simpson, C., & Eisenhardt, P. 1999, *PASP*, 111 691
 Smith, A.J., et al., 2012, *MNRAS*, 419, 377
 Newman, J. A. 2008, *ApJ*, 684, 88
 Waddington, I., et al. 2007, *MNRAS*, 381, 1437
 Wang, L., et al. 2011, published in *MNRAS*
 Wright, E.L., Eisenhardt, P., & Fazio, G. 1994, *BAAS*, 26, 893
 Zhang, P., Pen, U.-L., Bernstein, G. 2010, *MNRAS*, 405, 359